In-situ compression and electrochemical studies of graphene foam

*Correspondence:
SC: s_chaebi@yahoo.com

Sakineh Chabi[1,2,*], Esther Garcia-Tunon[3,4], Hongmei Chen[1,5], Yongde Xia[1], Eduardo G. Saiz[3], Yanqiu Zhu[1]

[1] College of Engineering, Mathematics and Physical Sciences, University of Exeter, Exeter EX4 4QF, United Kingdom
[2] Department of Mechanical Engineering, College of Engineering, Temple University, Philadelphia, Pennsylvania 19122, United States
[3] Centre for Advanced Structural Ceramics, Department of Materials, Imperial College London, London SW7 2AZ, United Kingdom
[4] Department of Mechanical, Materials and Aerospace Engineering, Materials Innovation Factory & School of Engineering, University of Liverpool, Liverpool L69 3GH, United Kingdom
[5] School of Materials Science and Engineering, Jiangsu University of Science and Technology, Zhenjiang Jiangsu 212003, China

Abstract

This study describes the correlation between structural, mechanical and electrochemical properties of graphene foam (GF) and focuses on the effects of 3D structure on the cycle life of graphene composite electrodes. The mechanical properties of the foam were assessed under in-situ compression tests within a scanning electron microscope. The foam showed a significant recovery after subjecting it to a compression strain exceeding 70%. The mechanical integrity and recoverability of the GF is related to its structural features, such as hollow struts, large size of the graphene sheets and low level of defects, all enabled the elastic deformation under compression loading. The advantage of the high flexibility and elasticity of these GFs was further explored and validated by using them as substrates for making composite materials for supercapacitor electrodes. Our findings indicated that the produced 3D GF-based composite have excellent cycle life and they do not show any capacity fading after thousands cycles of cyclic voltammetry test. This excellent performance is due to their ability to accommodate the cyclic strains during repeated charge-discharge cycles.

Introduction

Lightweight, highly flexible, highly conductive, strong and stretchable materials have always been pursued for advanced device constructions, and wood cellular, bones and shells are top examples of strong and highly ordered structures that exist in nature [1,2]. These materials offer unique properties in terms of high mechanical strength and low density. To create similar light and strong structures and apply those to device

fabrication industries, great efforts have been made to study the structures of these biological materials [3–7]. One successful technique to create such strong and light weight cellular structures is the two-step laser lithography and post atomic deposition method [8], which resulted in ultralight structures. The main rational behind this approach is to create ultrathin cell walls in the lattice, as the thin-walled nanolattice lowers the required weight for constructing robust structures [9]. These lightweight strong materials have been used for a wide range of applications *e.g.*, energy storage devices [10–12], new material fabrication [13,14], thermal conductivity enhancement [15], structural reinforcement [16], interface fielding [17], etc.

For use as energy storage materials, the electrode materials demand a high level of electronic and ionic conductance and flexibility that allows to accommodate the large cyclic strains during the repeated ion intercalation-extraction processes. Otherwise micro- and nano-cracks would form gradually which reduce the efficiency and are a major cause of the battery/capacitor failure. One of the most promising candidates for this purpose is graphene, because it possesses excellent electrical and mechanical properties and is the most stretchable crystal known to us. However, the true 2D graphene sheets have a flat structure with no pore or channels for ion transport, thus limiting their full potentials for direct applications for this purpose. New processes therefore have been developed to create channels and capillaries by ex-situ assembling the 2D sheets to form a 3D system. For example, nano capillary structures were formed based on Van der Waals force assisted assembly of 2D graphene sheets followed by a dry transfer technique [18]. The resulting structures, have a height of 0.34 N nm where N is the total numbers of graphene layer and 0.34 nm is the interlayer distance between graphene sheets, contain nanoscale cavities that allow for the transport of molecules and ions, whilst the capillary effect of the nanocavities could enhance the ion flow rates which improve the electrode efficiency. However, the integrity of the ex-situ constructed 3D graphene structures remains to be fully tested, as the adhesion only relies on the weak Van der Waals forces.

An ideal approach to allow for optimal ion transport within graphene materials is to design an intrinsically interconnected porous 3D graphene [19,20]. A specifically designed 3D GF with appropriate density range, pore size and distribution, and mechanical flexibility, on top of the excellent conductivity, could offer all the desired merits to achieve highly efficient electrodes with excellent cycle life and energy density. Some early studies using GFs either directly as the electrode or indirectly as the backbone structure in an electrode have exhibited very promising results. However, the direct contribution of mechanical properties (flexibility) of the GF to the cycle life of these electrodes has not been investigated. This level of understanding is crucial for device design and for achieving devices with optimal performance and efficiency.

This papers aims to demonstrate how the structural and mechanical properties of a 3D GF will influence the electrochemical performance when it is used as the backbone of a composite electrode. We will first investigate the in-situ compression behaviour of two types of ultralight GFs under SEM, and then validate and discuss how these GFs contribute to the improved performance of an electrochemical energy storage device.

Experimental section

GFs were synthesized by the CVD method, using a Ni foam (supplied by Novamet, USA, with a 99% porosity and 1.6 mm thickness) as the template and pure styrene (Sigma Aldrich >99%) as the carbon source. The synthesis procedure has been reported in our previous work [20]. SEM observations were performed using a Hitachi S3200N SEM-EDS machine. XRD powder diffraction patterns were recorded by a Bruker D8 Advance diffractometer working with a Cu-Kα radiation (λ = 0.154 nm) operated at 40 kV and 40 mA. The Raman spectra were collected on a Renishaw inVia Raman microscope, using a 532 nm wavelength excitation laser. Transmission electron microscopy (TEM) investigations were carried out using a JEM 2100 TEM (STEM), operated at 200 kV. For the TEM sample preparation, the samples were ultrasonically dispersed in acetone (Fisher Chemical) for 30 min and then the suspension was dropped onto a holey carbon coated copper grid (300 Mesh, Agar). The compression tests were carried out in situ inside a Hitachi S-3400N SEM, using a DEBEN microtest

with a 300 N single leadscrew tensile module. All tests were performed in a position controlled mode, at a speed of 0.001−0.6 mm/s, to record the morphological changes and elastic recovery of the structures. A CHI 660C Electrochemical Workstation and a three electrode cell was utilized for the electrochemical performance assessment. Pt was used as the auxiliary electrode, Ag/AgCl was the reference electrode and gold was used as the working electrode (2 mm diameter), and the measurements was carried out in a 0.5 M KCl (Sigma-Aldrich 99–100%) electrolyte. Cyclic voltammetry measurements were performed at a scan rate of 0.1 V s^{-1}.

Results and discussion

Figure 1 illustrates the preparation procedure and the morphology of the produced GFs. The mechanism for graphene growth on Ni substrate is believed to arise from carbon segregation which occurs during the cooling step and is a non-equilibrium process [21–23]. Macroscopically, the production of the Ni-templated GF follows the shape memory synthesis, in which the resulting foam keeps the original shape and dimensions of the Ni template. The as-produced GFs have an average dimension of 20 (L) × 20 (W) × 2 (H) mm^3. A high magnification image, Figure 1c, shows some wrinkles and ripples on the surface of the resulting GF. The wrinkles were formed mainly due to the difference in thermal expansion coefficients between the Ni and graphene. Microscopically, the resulting GF was made of large and curved 2D graphene layers, which was confirmed by imaging the collected flakes of the broken down GFs. Some of the large 2D pieces, as shown in Figure 1d, exhibited a size of 8 × 10 μm^2, which is fairly large indeed. Further TEM analyses revealed that the numbers of graphene layer in the flakes varied from 2–10. Figure 2 shows the results of XRD analysis and Raman spectroscopy of the GFs, and both confirmed the typical characteristics of multi-layered graphene. The intensity of the G peak at 1,580 cm^{-1} is higher than that of the 2D peak, with an $I_{2D}/I_G = 0.37$ (Figure 2b). The D peak, at about 1,350 cm^{-1}, is invisible, indicating the low level of
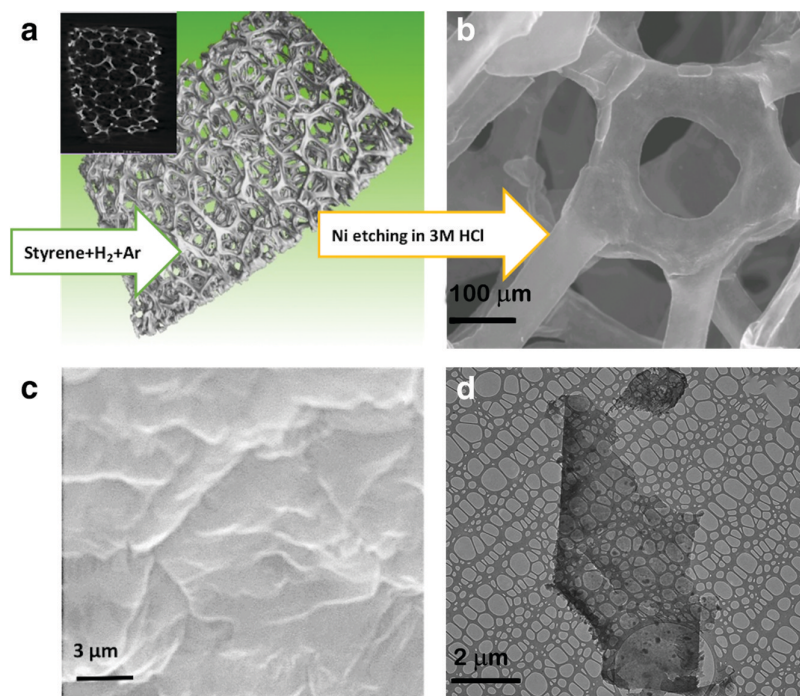
Figure 1. The preparation procedure of the GF and the morphology of the resulting GF. (a) μ-CT scan of the Ni foam template. The inset shows top view of the CT scan; (b) A SEM image of the GF after the Ni was leached out; (c) A high resolution SEM image of the GF showing the large area of graphene with many wrinkles; and (d) A TEM image of a large piece of graphene sheet collected after mechanically breaking down the GF.
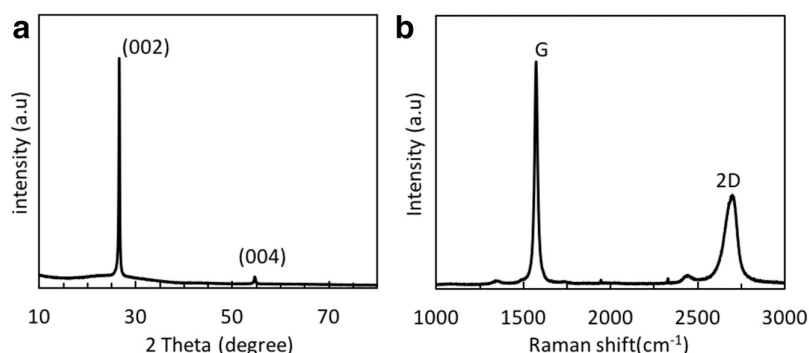
Figure 2. (a) XRD profile, and (b) Raman spectrum of the resulting GF.

defects and edges. These results confirm that the graphene quality for the 3D foam is high, and it is consistence with the large flake sizes observed above. The large flake sizes and low level of edge defects of the 2D graphene in the 3D GF would be expected to help enhance the electric and thermal conductivity, and benefit the mechanical integrity, of the GFs, against the 3D structural collapse and 2D sheet delamination.

In-situ investigation of the compression properties of the GF

The compression tests of the GFs were conducted within an SEM using in-situ SEM imaging to record the structure changes. GFs with a density range of 3–8 mg cm^{-3} were investigated under various compression loads. Figure 3 shows the sequential SEM images of a GF at different stages of testing.

Figure 3a shows an SEM image during the preparation stage of a very low density foam (ρ = 3 mg cm^{-3}) prior to the compression test. Under a maximum load of 3 N, Figure 3b, the sample became highly compressed and it underwent a 70% strain. Upon unloading, Figure 3c, the thickness of the GF increased again and the GF recovered significantly. At this magnification, the three snapshot images appeared to be similar, and the foam kept its original shape and general features, under different compression loads applied. However, at higher magnification, our observation revealed some cracks and micro-fractures in the foam, as shown in Figure 4. In these snapshot images, we have found that some individual beams underwent a partial damage and even collapse.

Figure 5 displays a typical individual beam during the compression and recovery steps. When an initial compression loads of 0.7 N was applied, the beam deviated from its original cylindrical shape and the strut buckled in the middle. Upon the removal of the load, the strut was partially recovered from this severely buckled status to a more relaxed state, however residue deformation remained and prohibited it from a full recovery.

As shown in both Figures 4 and 5, during the initial compression step when a load was applied, some micro cracks formed, however remained almost local until the end of the test. When the load was
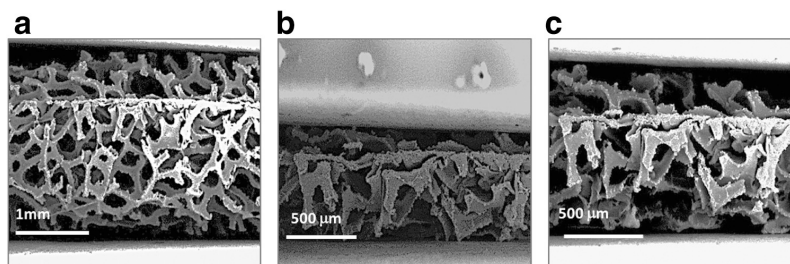

Figure 3. In-situ SEM images of GF$_a$ (ρ = 3 mg cm^{-3}) during the compression tests. (a) Before compression; (b) under a maximum load of 3N (70% strain), and (c) unloading stage (52% strain remains).
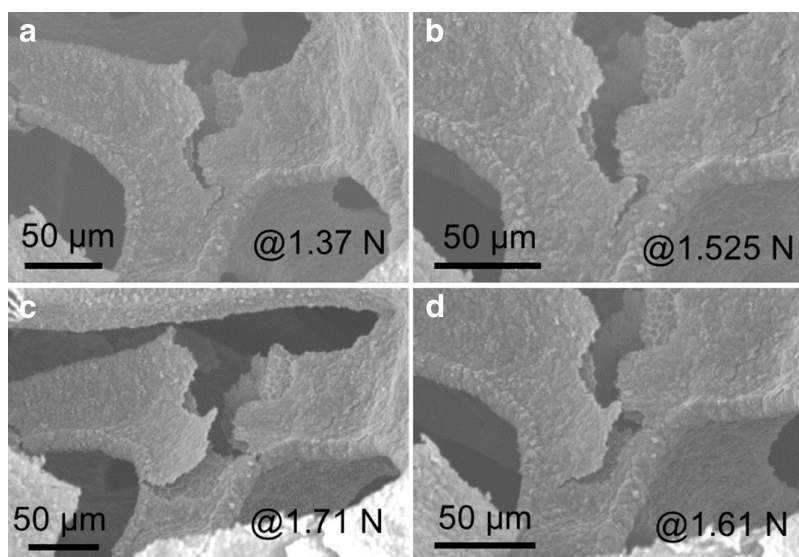
Figure 4. High magnification SEM images of GF under different compression loads. (a) 1.37 N, (b) 1.525 N, (c) 1.61 N, and (d) 1.71 N.

increased, the micro-cracks started to propagate slightly and spread locally, Figure 4, accompanied with the large structural deformation of entire structure. The combination of locally damaged and overall undamaged junctions contributed positively to hold the integrity of the foam, and allowed the foam to return to its original thickness.

Further, structural feature such as the interconnected porous network, the large sizes of the graphene sheets and the thin walls of the hollow struts, allowed for the localised buckling of individual struts under high compression load, therefore enabling the foam to realise sufficient flexibility for recovery and protecting the whole structure from dramatic collapse.
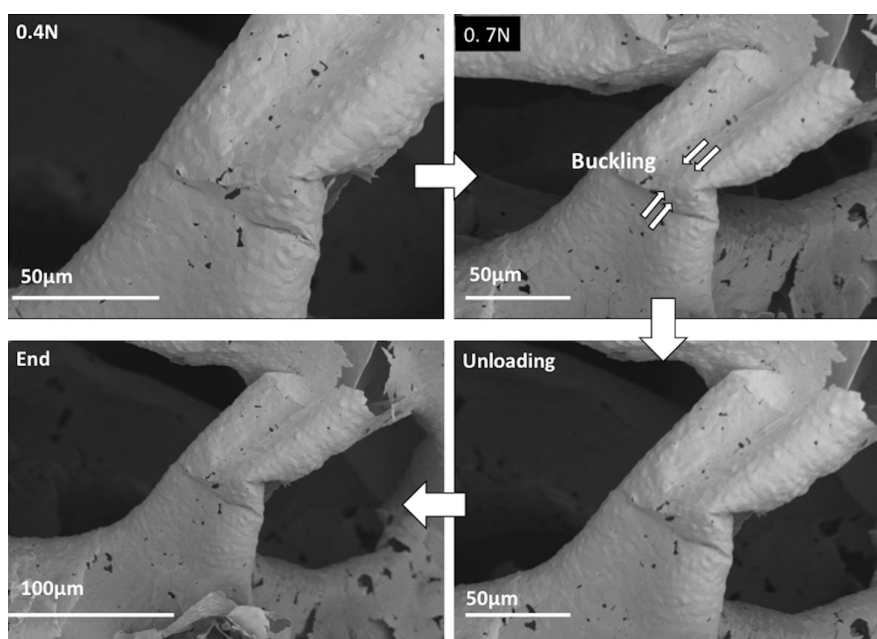

Figure 5. SEM image sequence of an individual beam under compression load of 0.4 N (16.3% strain), 0.7 N (31% strain), Unloading, and the End. Once the load was released, the beam partly recovered and 23% of the strain remains.

Depending on the microstructure, *e.g.*, orientation, defects, porosity, and density, the GFs behave differently during the unloading stage. Our characterised GFs show a different level of recovery, due to their structural differences. For example, the foam shown in Figures S1–S2 exhibited significant recovery feature, where a 82% recovery was recorded in the SEM image and only 18% strain remained.

The effects of density on the compression strength of the GFs were also investigated. Figure 6 shows the compression stress-strain curves of two GFs of different density values: GF_a (ρ = 3 mg cm^{-3}) and GF_b (ρ = 7 mg cm^{-3}). Basically, both curves exhibit a typical stress-strain response of open cell foams, with a large plateau region followed by a sudden densification. In the densification regions the stresses rise steeply, and it is likely that the struts experienced collapsing, the large graphene flakes impinged upon each other, and the entire structure was densified and suffered from permanent damage.

Compared with GF_a, GF_b showed a slightly higher compressive strength, which is due to the higher density of the latter. The higher density of GF_b is originated from the thicker walls of its struts than those of GF_a. The walls of these struts are consisted of large or even continuous few layered graphene sheets as shown earlier, and these sheets were held together *via* π-π interaction [24]. Therefore, within the tested very low density range, the more layers in the struts the higher the compression strength. Furthermore, based on the stress-strain data in Figure 6b, a compression strength of about 20 kPa was also obtained for GF_b, which is superior to most of the existing lightweight carbon foams (with density values less than 10 mg cm^{-3}) [24–31].

Manifestations of the mechanical integrity of the graphene-polymer composites during potential cycling

Conductive polymers such as polypyrrole (PPY), are known for their high charge capacity, and they are widely used for supercapacitor application. However, they suffer from poor cycle life since they can barely sustain their initial current and performance after repeated charge-discharge cycles. One solution for this problem is to deposit the polymer on a robust and conductive scaffold. Therefore, the combination of PPY with the potentially conductive and yet flexible 3D GF offers an ideal way to pursue this understanding mentioned above.

Figure 7 shows the results of cyclic voltammetry measurements of the GF, plain PPY, and the PPY-GF composite. The specific capacitance may be calculated from $C_m = \dfrac{I \times t}{m \times V}$, where C_m is the specific capacitance, I is the current, t is the discharge time, V is the voltage windows and m is the weight of the electrode materials. We obtained values of 3.5, 414 and 660 F g^{-1} as specific capacitance (initial capacitance) of GF, PPY, and PPY-GF electrodes [20]. The specific capacitance of both PPY and PPY-GF is quite high, however the challenge is to maintain this performance for a long time.

As shown in Figure 7b, the first and the 10,000th cycles of the CV measurement of the GF overlap each other completely, *i.e.*, the current values in the first cycle are the same as in the 10,000th cycle, although the values are very low, only 50 mA g^{-1}. In the case of PPY, Figure 7d, the initial current, although
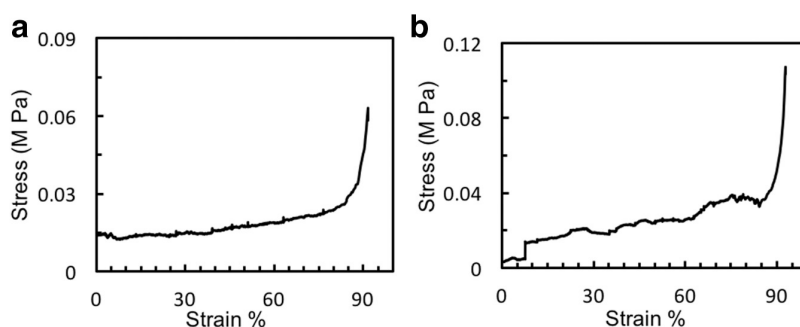

Figure 6. Stress-strain curves of two different GFs; GF_a (ρ = 3 mg cm^{-3}) and GF_b (ρ = 7 mg cm^{-3}).
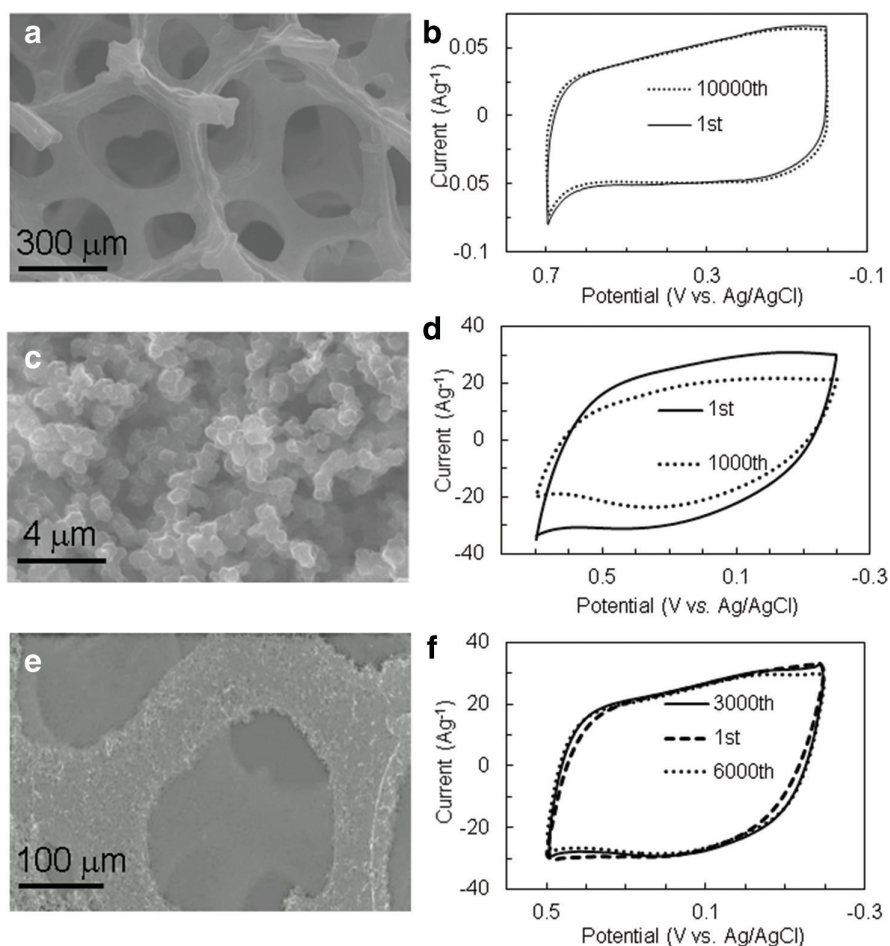
Figure 7. Representative SEM morphologies of different electrodes and their corresponding Cyclic Voltammetry results. (a, b) Pure GF, (c, d) Plain PPY, (e, f) PPY-GF composite.

high, suffers a 30% loss after only 1,000 cycles. The PPY-GF composite, similar to the GF, maintains its initial high current after 6,000 cycles, Figure 7f.

The significant differences in cycle life of the three electrodes are originated from the GFs, as both the plain GF and PPY-GF composite electrodes demonstrated excellent cycle life and maintained their initial currents.

During each cycle of the CV test, the ions from the electrolyte get intercalated-extracted into and out the electrode materials, causing a volume expansion and shrinkage cycle to the electrode materials which results in cyclic stresses. Sustained stresses could gradually lead to microcrack formation which degrade the conductivity and eventually lead to failure. Therefore, the electrode materials are highly desirable to have the flexibility, strength and void capacity to cope with such repeated volume changes (extension-contraction) during prolonged cycles, without cracks formation and performance degradation.

Pure PPY can only cope with such volume change for a few cycles before losing its integrity, since it is poorly shaped and aggregated from isolated particles, as shown in Figure 7c. Indeed, when using PPY as the electrode materials, the aggregates quickly form cracks and lose their mechanical integrity, and even possibly partly fell off from the substrate and dropped into the electrolyte, after limited number of CV cycles, therefore we observed current decreases with increased cycling. On the contrary, when combined with the highly flexible GF as the backbone, the PPY in the PPY-GF composite electrode can be stabilized by the 3D GF scaffold, as shown in Figure 7e, and the PPY particles attached to GF surface can recover and maintain their initial configuration after thousands of cycles.

As discussed earlier, the GF was able to recover significantly and retain its original shape after subjecting to a compression load as high as 3 N, and this high strength is beneficial here. Furthermore, the flexible GF also acted as an effective holder to uniformly distribute the stress concentrations that raised within the PPY from each charge-discharge cycle. The open porosity feature of the foam was very helpful in stabilizing the surface morphology of the highly conductive PPY redox counterpart, as the pores can function as a host to the redox elements and accommodate the strains in the entire electrode structure during repeated cycling.

We believe that the ultralow density and high porous nature of the foam played a very important role in the excellent flexibility, because the hollow feature of both the struts and the overall form allowed the GFs to deform via different bending, tilting, stretching, and buckling modes, to absorb and easy off local concentrated stresses, therefore avoiding massive damage or structure collapse.

Conclusion

In summary, we have investigated the compression behavior of ultralight GF under SEM observation. The foams did not crash under the applied load, instead they kept their original 3D shape and only compacted. The results reveal that structural features, such as the low defect graphene, very large graphene sheet and ultrathin wall (only few layer graphene), and the porous network of the foam, have all contributed positively to the mechanical integrity of the foam and resulted in elastic buckling response and ultimately significant recovery upon removing the load. Owing to its high flexibility and open porosity feature, the produced GF, and graphene-polymer composites, have shown excellent cycle life and 100% capacity retention after thousands of charge-discharge cycles.

Supporting material

S1. In situ compression and electrochemical studies of graphene foam. (DOCX)

Acknowledgements

Competing interests

The authors state that they have no conflict of interest. Yanqiu Zhu is the Editor-in-Chief of Veruscript Functional Nanomaterials. He would like to disclose that an Associate Editor took full responsibility for the handling of the peer review process on this article.

References

1. Varela-Feria F., Martínez-Fernández J., de Arellano-López A., and Singh M. Low density biomorphic silicon carbide: microstructure and mechanical properties. Journal of the European Ceramic Society. 2002; 22 (14–15): 2719–2725. https://doi.org/10.1016/S0955-2219(02)00137-1.

2. Shin Y., Liu J., Chang J. H., Nie Z., and Exarhos G. J. Hierarchically ordered ceramics through surfactant-templated sol-gel mineralization of biological cellular structures. Advanced Materials. 2001; 13 (10): 728–732. https://doi.org/10.1002/1521-4095(200105)13:10<728::AID-ADMA728>3.0.CO;2-J.

3. Xu Z., Zhang Y., Li P., and Gao C. Strong, conductive, lightweight, neat graphene aerogel fibers with aligned pores. ACS Nano. 2012; 6 (8): 7103–7113. https://doi.org/10.1021/nn3021772.

4. Leventis N. Three-dimensional core-shell superstructures: Mechanically strong aerogels. Accounts of Chemical Research. 2007; 40 (9): 874–884. https://doi.org/10.1021/ar600033s.

5. Liu T., Deng Z. C., and Lu T. J. Structural modeling of sandwich structures with lightweight cellular cores. Acta Mechanica Sinica. 2007; 23 (5): 545–559. https://doi.org/10.1007/s10409-007-0096-z.

6. Yu R., Ching K.-L., Lin Q., Leung S.-F., Arcrossito D., et al. Strong light absorption of self-organized 3-D nanospike arrays for photovoltaic applications. ACS Nano. 2011; 5 (11): 9291–9298. https://doi.org/10.1021/nn203844z.

7. Ji H., Zhang L., Pettes M. T., Li H., Chen S., et al. Ultrathin graphite foam: A three-dimensional conductive network for battery electrodes. Nano Letters. 2012; 12 (5): 2446–2451. https://doi.org/10.1021/nl300528p.

8. Schaedler T. A., Jacobsen A. J., Torrents A., Sorensen A. E., Lian J., et al. Ultralight metallic microlattices. Science. 2011; 334 (6058): 962–965. https://doi.org/10.1126/science.1211649.

9. Meza L. R., Das S., and Greer J. R. Strong, lightweight, and recoverable three-dimensional ceramic nanolattices. Science. 2014; 345 (6202): 1322–1326. https://doi.org/10.1126/science.1255908.

10. Bi H., Lin T., Xu F., Tang Y., Liu Z., et al. New graphene form of nanoporous monolith for excellent energy storage. Nano Letters. 2016; 16 (1): 349–354. https://doi.org/10.1021/acs.nanolett.5b03923.

11. Hu G., Xu C., Sun Z., Wang S., Cheng H. M., et al. 3D graphene-foam-reduced-graphene-oxide hybrid nested hierarchical networks for high-performance Li-S batteries. Advanced Materials. 2016; 28 (8): 1603–1609. https://doi.org/10.1002/adma.201504765.

12. Zhang Z., Xiao F., Qian L., Xiao J., Wang S., et al. Facile synthesis of 3D MnO_2-graphene and carbon nanotube-graphene composite networks for high-performance, flexible, all-solid-state asymmetric supercapacitors. Advanced Energy Materials. 2014; 4 (10): 1400064 (1–9). https://doi.org/10.1002/aenm.201400064.

13. Chabi S., Rocha V. G., García-Tunon E., Ferraro C., Saiz E., et al. Ultralight, strong, three-dimensional SiC structures. ACS Nano. 2016; 10 (2): 1871–1876. https://doi.org/10.1021/acsnano.5b05533.

14. Chabi S., Chang H., Xia Y., and Zhu Y. From graphene to silicon carbide: Ultrathin silicon carbide flakes. Nanotechnology. 2016; 27 (7): 075602. https://doi.org/10.1088/0957-4484/27/7/075602.

15. Alam F. E., Dai W., Yang M., Du S., Li X., et al. In situ formation of a cellular graphene framework in thermoplastic composites leading to superior thermal conductivity. Journal of Materials Chemistry A. 2017; 5 (13): 6164–6169. https://doi.org/10.1039/C7TA00750G.

16. Shi J., Li X., Cheng H., Liu Z., Zhao L., et al. Graphene reinforced carbon nanotube networks for wearable strain sensors. Advanced Functional Materials. 2016; 26: 2078–2084. https://doi.org/10.1002/adfm.201504804.

17. Ling J., Zhai W., Feng W., Shen B., Zhang J., et al. Facile preparation of lightweight microcellular polyetherimide/graphene composite foams for electromagnetic interference shielding. ACS Applied Materials & Interfaces. 2013; 5 (7): 2677–2684. https://doi.org/10.1021/am303289m.

18. Radha B., Esfandiar A., Wang F. C., Rooney A. P., Gopinadhan K., et al. Molecular transport through capillaries made with atomic-scale precision. Nature. 2016; 538 (7624): 222–225. https://doi.org/10.1038/nature19363.

19. Chen Z., Ren W., Gao L., Liu B., Pei S., et al. Three-dimensional flexible and conductive interconnected graphene networks grown by chemical vapour deposition. Nature Materials. 2011; 10 (6): 424–428. https://doi.org/10.1038/nmat3001.

20. Chabi S., Peng C., Yang Z., Xia Y., and Zhu Y. Three dimensional (3D) flexible graphene foam/polypyrrole composite: Towards highly efficient supercapacitors. RSC Advances. 2015; 5 (6): 3999–4008. https://doi.org/10.1039/C4RA13743D.

21. Chae S. J., Günes F., Kim K. K., Kim E. S., Han G. H., et al. Synthesis of large-area graphene layers on poly-nickel substrate by chemical vapor deposition: Wrinkle formation. Advanced Materials. 2009; 21: 2328–2333. https://doi.org/10.1002/adma.200803016.

22. Yu Q., Lian J., Siriponglert S., Li H., Chen Y. P., et al. Graphene segregated on Ni surfaces and transferred to insulators. Applied Physics Letters. 2008; 93: 113103. https://doi.org/10.1063/1.2982585.

23. Naseem H. CVD graphene growth mechanism on nickel thin films. Proceedings of the 2014 COMSOL Conference in Boston. 2014; 446: 7131.

24. Li Y., Chen J., Huang L., Li C., Hong J. D., et al. Highly compressible macroporous graphene monoliths via an improved hydrothermal process. Advanced Materials. 2014; 26 (28): 4789–4793. https://doi.org/10.1002/adma.201400657.

25. Samad Y. A., Li Y., Schiffer A., Alhassan S. M., and Liao K. Graphene foam developed with a novel two-step technique for low and high strains and pressure-sensing applications. Small. 2015; 11 (20): 2380–2385. https://doi.org/10.1002/smll.201403532.

26. Sun H., Xu Z., and Gao C. Multifunctional, ultra-flyweight, synergistically assembled carbon aerogels. Advanced Materials. 2013; 25 (18): 2554–2560. https://doi.org/10.1002/adma.201204576.

27. Si Y., Yu J., Tang X., Ge J., and Ding B. Ultralight nanofibre-assembled cellular aerogels with superelasticity and multifunctionality. Nature Communications. 2014; 5: 5802. https://doi.org/10.1038/ncomms6802.

28. Yin J., Li X., Zhou J., and Guo W. Ultralight three-dimensional boron nitride foam with ultralow permittivity and superelasticity. Nano Letters. 2013; 13 (7): 3232–3236. https://doi.org/10.1021/nl401308v.

29. Zou J., Liu J., Karakoti A. S., Kumar A., Joung D., et al. Ultralight multiwalled carbon nanotube aerogel. ACS Nano. 2010; 4 (12): 7293–7302. https://doi.org/10.1021/nn102246a.

30. Qiu L., Liu J. Z., Chang S. L. Y., Wu Y., and Li D. Biomimetic superelastic graphene-based cellular monoliths. Nature Communications. 2012; 3: 1241. https://doi.org/10.1038/ncomms2251.

31. Gui X., Wei J., Wang K., Cao A., Zhu H., et al. Carbon nanotube sponges. Advanced Materials. 2010; 22 (5): 617–621. https://doi.org/10.1002/adma.200902986.